Journal of Power Sources 588 (2023) 233745

Contents lists available at ScienceDirect

Journal of Power Sources

journal homepage: www.elsevier.com/locate/jpowsour

Cracking and associated volumetric expansion of NMC811 secondary particles

S.S. Shishvan [a,b], N.A. Fleck [b], R.M. McMeeking [c,d,e], V.S. Deshpande [b,*]

[a] Department of Structural Engineering, University of Tabriz, Tabriz, Iran
[b] Department of Engineering, University of Cambridge, Cambridg, CB2 1PZ, UK
[c] Departments of Materials and Mechanical Engineering, University of California, Santa Barbara, CA, 93106, USA
[d] School of Engineering, University of Aberdeen, King's College, Aberdeen, AB24 3UE, UK
[e] INM-Leibniz Institute for New Materials, Campus D2 2, 66123, Saarbrücken, Germany

HIGHLIGHTS

- A framework is developed to model the fracture of NMC811 secondary particles.
- Fragmentation is predicted in the absence of Li concentration gradients.
- Volumetric expansion of the secondary particles upon cracking is predicted.
- The dynamic nature of the cracking event during delithiation is emphasised.
- Predictions are in agreement with observations.

ARTICLE INFO

Keywords:
Li-ion battery
Ni-rich NMC cathodes
Secondary particle
Cracking
Modelling

ABSTRACT

Secondary particles comprising a large number of nickel-rich single crystal primary particles are extensively used as storage particles in cathodes of lithium-ion batteries. It is well-established that crack formation in secondary particles is an important degradation mode that contributes to decline in battery performance. Recent X-ray tomographic observations suggest that, at very low C-rates, concentration gradients of lithium within an NMC811 secondary particle are negligible yet cracking still occurs. Additionally, during delithiation the primary particles shrink yet a volumetric expansion of the secondary particle occurs. These observations are explained by a numerical model of distributed cracking due to the extreme anisotropy of lithiation strain of primary particles. The incompatible deformation from grain to grain induces large self-stresses even in the absence of spatial gradients in the lithium concentration. The stress state is sufficient to drive a dynamic catastrophic fracture event, and the associated kinetic energy acquired by the primary particles moves them apart (akin to an explosive event) with the carbon and binder domain surrounding each secondary particle restricting the outward motion of the primary particles. It is predicted that a volume expansion of the secondary particles on the order of 20 % accompanies cracking, in agreement with recently reported observations.

1. Introduction

Rapid advances in Lithium-Ion Battery (LIB) technology include next-generation cathodes that comprise layered, Nickel-rich Manganese Cobalt (NMC) materials. Compared to the more traditional Lithium Cobalt Oxide (LCO), nickel-rich NMC ($LiNi_pMn_qCo_rO_2$, where $p + q + r = 1$, $p \geq 0.5$) contains less of the rare and expensive element cobalt. The alloy $LiNi_{0.8}Mn_{0.1}Co_{0.1}O_2$ (known as NMC811) is one such candidate due to its high specific energy storage capacity [1]. Polycrystalline agglomerates (termed secondary particles) of single crystals (termed primary particles) are commonly used for Li storage in order to achieve a high volume fraction of active material in the cathode. However, it is well established that secondary particles of NMC (and of LCO) crack upon cell cycling: cracking of secondary particles can reduce performance by (i) reducing electrical connection between particles and the conductive architecture in the electrode matrix, and (ii) oxygen release

* Corresponding author.
E-mail address: vsd20@cam.ac.uk (V.S. Deshpande).

https://doi.org/10.1016/j.jpowsour.2023.233745
Received 8 August 2023; Received in revised form 30 September 2023; Accepted 14 October 2023
Available online 20 October 2023

at fresh surface leading to electrolyte oxidation. Thus, the interplay between mechanics and electrochemistry in stress generation within secondary particles and their associated cracking has been extensively investigated; see recent reviews [2–4].

The majority of models [3], which were developed for traditional cathode materials such as $Li_xMn_2O_4$ and $LiCoO_2$, assume an isotropic response of the storage particles. The generation of stress and associated cracking in these models can be understood as follows. At a finite charging rate, the lithiation/delithiation causes a non-uniform volume change of the material within the particle which results in generation of self-stress, analogous to the stresses induced by non-uniform thermal strain [5,6]. For example, Purkayastha and McMeeking [7,8] carried out simulations on the stress state generated in spherical secondary particles when intercalated at a constant rate of extraction from the surface. They developed maps of the stress level generated as a function of extraction rate, particle size and material properties and showed that the level of stress generated is high when extraction is rapid, the particle is large, solid-state diffusion is slow, a large molar volume of lithium is extracted, the elastic modulus is high, and the lithium storage capacity is large. The above studies address lithiation/delithiation of a storage particle without explicit consideration of the presence of cracks. Woodford et al. [9] derived a fracture mechanics failure criterion for individual electrode particles by calculating the stress intensity factor along the front of a thumbnail-shaped surface crack. They produced a map that shows regimes of failure depending upon charge and discharge rate, particle size, and fracture toughness of the secondary particle. The propensity for fracture increases with increasing charging rate, particle size and decreasing fracture toughness. Subsequently, they extended these ideas to single- and polycrystals [10] and to phase transforming materials [11].

While above mentioned studies have been successful in modelling the cracking of $Li_xMn_2O_4$ and $LiCoO_2$, the important differences are being reported in the mechanisms and conditions under which NMC secondary particles fracture. Kondarkov et al. [12] reported that NMC811 secondary particles undergo large and irreversible size changes (without quantifying them) during the first cycle at a charging rate of C/10. Li et al. [13] used nano-tomography to observe the cracking of NMC811 secondary particles upon delithiation at C/ 5 and reported the porosity generation in the range 12% to 24% in the fully delithiated secondary particle. More direct and quantitative observations of the same phenomenon have been recently reported by Parks et al. [14] for delithiation at C/50. Specifically, they reported that NMC811 secondary particles of diameter in the range 10 μm to 18 μm extensively crack when delithiated at C/50 and this cracking is accompanied by a $\sim$20% volumetric expansion of the secondary particles; see Fig. 1. Thus, the models discussed above which require Li spatial gradients to initiate cracking are unable to predict cracking of NMC secondary particles that occurs at low C-rates. An even more surprising observation is that cracking of NMC811 upon delithiation is accompanied by volume expansion [12–14]. To understand this, recall that the lithiation strains of NMC811 single crystals are highly anisotropic and vary non-linearly with the lithium occupancy [15,16]. Briefly, upon delithiation the strains along the a and b directions (the $a-b$ plane is the basal plane of the NMC crystal) are equal and decrease monotonically with decreasing lithium occupancy while the c direction strain initially increases with decreasing lithium occupancy and then decreases. However, the volumetric strain of the NMC811 single crystal decreases monotonically upon delithiation and the single crystal has approximately a 6 % lower volume upon complete delithiation compared to its fully lithiated state. Given that each NMC811 primary particle shrinks upon delithiation, it is surprising that the secondary particle expands upon cracking during delithiation.

The crack paths in most secondary particles are complicated similar to the cracking patterns shown in Fig. 1 for NMC811. Given these complexities, there have been efforts to eliminate or reduce the influence of the finite element mesh used in computations that predict

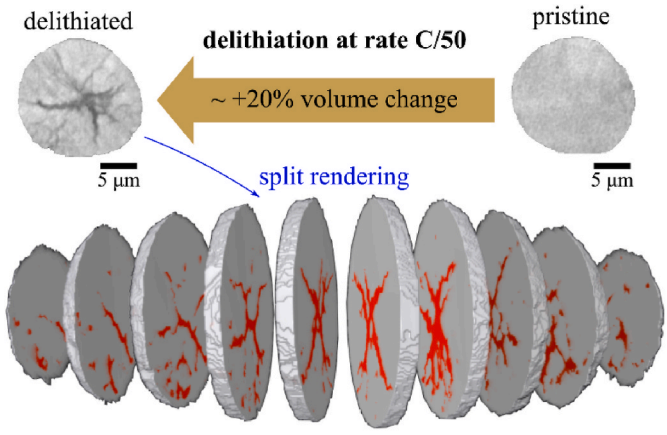

Fig. 1. Cracking of NMC811 secondary particles delithiated at C/50; reproduced in part and in schematic form from Ref. [14]. A tomographic slice through the mid-section of an approximately spherical NMC811 secondary particle reveals cracking due to delithiation. X-ray tomographic reconstructions show slices through the fractured particle in split rendering; cracks detected by the tomography are coloured red. There is a substantial number of additional cracks below the resolution of the tomography. The fractured particle has expanded by $\sim$ 20% from its initial pristine state. (For interpretation of the references to colour in this figure legend, the reader is referred to the Web version of this article.)

cracking patterns. For example, Zhu et al. [17] used an extended finite element method known as XFEM, Sun et al. [18] and Li et al. [13] used a cohesive zone approach, Allen et al. [19] used a 3D continuum level damage model to study effects of particle architectures, and Klinsmann et al. [20] and Parks et al. [14] exploited the phase field fracture method to permit greater versatility of potential crack path. While these studies model a single particle, there exist studies that construct a (mesoscale) model of electrode containing multiple particles [21,22]. None of these studies address the expansion of the secondary particles during the cracking which is the main goal of the present study.

Here, we present a theoretical framework for cracking and volumetric expansion of NMC811 secondary particles. We restrict consideration to the case of low C-rate where spatial gradients of lithium concentration are absent. While we recognise that these low C-rates unlikely to be of practical interest [23], they represent the simplest and cleanest way to understand the volume expansion of the secondary particles as recognised in recent experimental studies [12–14]: this is the primary aim of this study. We explicitly model the polycrystalline assembly of the single crystal primary particles that form the secondary particle with intergranular fracture modelled by cohesive zones. The dynamic nature of the cracking event is emphasised. Volumetric expansion of the secondary particles upon cracking is traced to the phenomenon of dynamic cracking.

2. Materials and methods

We develop a framework to model the fracture of secondary particles within a composite cathode. The focus is on fracture at low C-rates where the Li concentration within the secondary particle is spatially uniform. In this limit, the mechanical and electrochemical effects are decoupled which simplifies the model including removing the need to explicitly consider the solid-electrolyte interface (SEI). Consider a spherical secondary particle of radius R_P comprising randomly shaped and oriented single crystal grains (primary particles), with faces comprising approximately flat facets: the grains are all approximately of the same size with a leading dimension d (Fig. 2a). We assume that the pristine secondary particle is free of both porosity and cracks in the initial sintered state and comprises fully lithiated primary particles that are all well-bonded. This ideal case provides a limit on the fracture

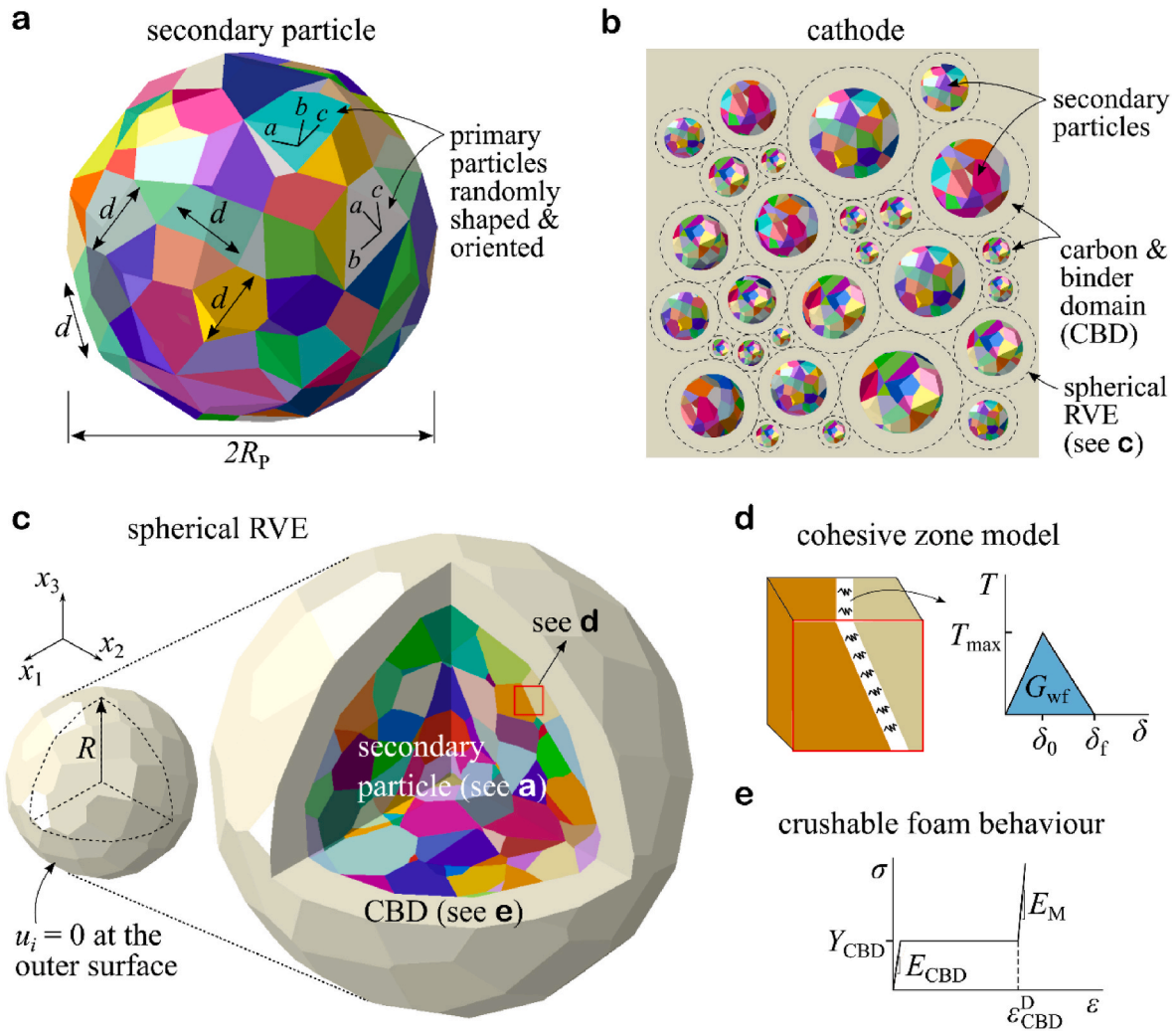

Fig. 2. (a) Rendering of the spherical secondary particle of radius R_P used in the numerical calculations. The particle comprises N randomly oriented and shaped single crystal primary particles of average size d. The primary grains are coloured to differentiate them and the crystallographic axes (a, b, c) are labelled on selected grains to indicate their orientation. (b) The cathode comprising randomly distributed secondary particles within the CBD. The cathode is modelled via the composite sphere model [24] and the RVE indicated by dashed lines. (c) Sketch of the spherical RVE used in the analysis with the imposed boundary conditions. The global Cartesian co-ordinate system is also shown. Sketches of (d) the intergranular cohesive zone model (see Appendix A) and (e) the uniaxial behaviour of the CBD (see Appendix B).

performance of the secondary particle. The secondary particles are embedded within the cathode matrix of porous polymer binder through which the liquid electrolyte permeates and carbon particles to conduct electrons to the current collector. We shall refer to this porous mixture (Fig. 2b) as the carbon and binder domain (CBD).

The composite cathode comprises a volume fraction f_P of the secondary particles and f_V of voids (filled with liquid electrolyte) so that a fraction $[1-(f_P+f_V)]$ is occupied by the polymer binder material and carbon while the porous CBD occupies a volume fraction $(1-f_P)$. The cathode is therefore a particulate composite (Fig. 2b), and to analyse the fracture response of the secondary particles, we resort to analyses extensively used to model the mechanical behaviour of particulate composites. Hashin's composite sphere model [24] is particularly suited to model a high-volume fraction particulate composite akin to the cathode. In this model, the representative volume element (RVE) is a composite sphere comprising an inner core of the spherical secondary particle of radius R_P and an outer concentric shell of radius $R = R_P/f_P^{1/3}$ that represents the CBD (Fig. 2c). The assembly of such composite spheres is space filling as it is assumed that there is a distribution of RVE sizes but with each RVE satisfying $f_P = (R_P/R)^3$ (Fig. 2b). In order to make contact with recent experimental observations [14], we shall focus on a composite cathode comprising NMC811 secondary particles that are delithaited at C/50; consequently, spatial Li gradients are absent within each secondary particle.

2.1. Model for the secondary particle

The secondary particle with radius R_P comprises N single crystal NMC811 grains with random shapes and orientations (Fig. 2a). This polycrystalline secondary particle was constructed in Neper [25] with the N primary grains generated via a Poisson-Voronoi tessellation and the spherical surface of the secondary particle was discretised by 48 planes. A *regularisation* step was applied whereby slightly non-planar internal grain facets were permitted to ensure that no grains have faces with edges of length $< 0.02R_P$. This ensured that all primary grains had realistic shapes and it also helped improve the quality of the finite element (FE) mesh used in the calculations. A characteristic grain size can then be defined as follows. Given a grain has a volume V_g, its size is characterized by the diameter of sphere of equal volume, i.e., a characteristic grain size follows $d_g = 2[3V_g/(4\pi)]^{1/3}$. Equivalently, the average grain size within the secondary particle is denoted by d and specified by $2R_P/N^{1/3}$.

The intergranular bonding between the grains was modelled using a mixed-mode cohesive zone formulation (see Fig. 2d with additional details of the formulation provided in Appendix A). The cohesive zone is such that the mode II and mode III toughness are both equal to the mode I toughness. Intergranular bonding is characterised by two parameters: the cohesive strength $T_{\max}$ and the intergranular fracture energy $G_{\rm wf}$. In keeping with the known brittle nature of the fracture of the NMC secondary particle, we choose these parameters so that fracture is governed by $G_{\rm wf}$ such that $T_{\max}$ only serves as a numerical regularisation parameter as explained in Section 2.4. After fracture, interactions between the single crystal grains are modelled via a contact analysis wherein interpenetration of the grains is prevented and sliding between the grains is governed by a Coulomb friction relation with a friction co-efficient μ. Calculations are reported for three random realisations of the secondary particle to illustrate the effect of statistical variability associated with the distributions of the primary grain orientations within the secondary particle.

Each NMC811 primary grain within the secondary particle is modelled as a transversely isotropic single crystal with the plane of isotropy coinciding with the basal plane of the NMC crystal. Following [26], the five elastic constants are assumed to be independent of Li content. Using Cartesian tensor notation and the fixed global Cartesian co-ordinate system indicated in Fig. 2c, the Cauchy stress σ_{ij} is related to the elastic strain $\varepsilon^{\rm EL}_{ij}$ via $\sigma_{ij} = C_{ijkl}\varepsilon^{\rm EL}_{kl}$ where C_{ijkl} is the fourth order elastic modulus tensor. The total strain ε_{ij} of each crystal is the symmetric part of the gradient of the displacement field u_i such that $\varepsilon_{ij} \equiv (u_{i,j} + u_{j,i})/2$. The total strain is additively decomposed into the elastic strain and the lattice strain $\varepsilon^{\theta}_{ij}$ due to the intercalation of the Li ions into the NMC811 unit cell, giving $\varepsilon_{ij} = \varepsilon^{\rm EL}_{ij} + \varepsilon^{\theta}_{ij}$. Let (a, b, c) denote an orthogonal crystal co-ordinate system (c.f. Fig. 2a) where the ab-plane is the basal plane of the NMC crystal and the c-axis is perpendicular to this basal plane. Then, the lithiation strain in the crystallographic basis (a, b, c) is

$$\boldsymbol{\varepsilon}^{\theta} = \begin{bmatrix} \varepsilon^{\theta}_{a}(\theta) & 0 & 0 \\ 0 & \varepsilon^{\theta}_{b}(\theta) & 0 \\ 0 & 0 & \varepsilon^{\theta}_{c}(\theta) \end{bmatrix}, \tag{1}$$

where ε^{θ}_{a}, ε^{θ}_{b} and ε^{θ}_{c} are the lattice strain components along the a, b and c axes, respectively, that are functions of the occupancy $0 \le \theta \le 1$ of the available Li sites within the NMC unit cell. These lithiation strains have been measured by X-ray diffraction and by other methods [15,16]. The stress state within the polycrystalline assembly of randomly oriented grains is fully described by their elastic law involving the lithiation strains as well as the intergranular interactions parameterised via the cohesive zone framework, with due account of equilibrium and compatibility. Hard contact between grains with Columbic friction governs the interactions between the fractured grains.

2.2. Model for the CBD

The RVE comprises a secondary particle and a concentric shell of CBD (Fig. 2c). Recall that the CBD is a mixture of porous binder and carbon, with liquid electrolyte able to percolate through the interconnected porosity of the binder. However, our focus here is to model the fracture of the secondary particles and thus to simplify the numerical description of the CBD we homogenise the three phases of the CBD. We model the porous CBD as a crushable foam with a zero plastic Poisson's ratio using the Deshpande-Fleck [27,28] foam constitutive model that is detailed in Appendix B. Briefly the isotropic CBD is parametrised by an initial elastic region described by a Young's modulus $E_{\rm CBD}$ and Poisson's ratio $\nu_{\rm CBD}$ while the plastic behaviour is characterised by a uniaxial crushing strength $Y_{\rm CBD}$ and a uniaxial densification strain $\varepsilon^{\rm D}_{\rm CBD}$ at which the crushing is arrested (Fig. 2e). The true compressive densification strain is related to the porosity $\rho_{\rm V} = f_{\rm V}/(1 - f_{\rm P})$ of the CBD via $\varepsilon^{\rm D}_{\rm CBD} = 0.8\rho_{\rm V}$ [29].

2.3. Imposed loading and boundary conditions

We impose overall cathode boundary conditions on the RVE and therefore fix all displacements on the outer radius R of the composite sphere (Fig. 2c). This is equivalent to an upper bound analysis in the context of the Hashin composite sphere model [24] and give a lower bound on the expansion of the secondary particle. Delithiation of the cathode at a C/50 rate is imposed. This rate is sufficiently slow compared to the time-scale for the diffusion of Li within the secondary particle thus it is reasonable to assume that the Li occupancy fraction θ within the secondary particle is spatially uniform. In the calculations, we thus specify θ as a function of time (with θ being spatially uniform within the entire secondary particle) such that $\theta = 1$ at time $t = 0$ (the pristine secondary particle is fully lithiated) and $\theta = 0.1$ at the end of delithiation at time $t_{\rm e}$. No other mechanical or other type loads are imposed on the RVE. The differential lithiation strain from one primary particle to the next generates significant deformation and stress within the secondary particle.

2.4. Material properties

The five independent elastic constants of the transversely isotropic NMC811 single crystal are most conveniently specified in the crystallographic basis (a, b, c). These are taken from Ref. [30] and are listed in Table 1 in terms of the Young's modulus E_a in the ab-plane, the Young's modulus E_c along the c-axis, the shear modulus G_{ac} in the ac-plane and the two Poisson's ratios $\nu_{ab} \equiv -\varepsilon^{\rm EL}_{b}/\varepsilon^{\rm EL}_{a}$ and $\nu_{ac} \equiv -\varepsilon^{\rm EL}_{c}/\varepsilon^{\rm EL}_{a}$, where $\varepsilon^{\rm EL}_{\rm x}$ is the direct elastic strain in the x crystallographic direction. Given the orientation of a primary particle with respect to the global co-ordinate system, these five constants can be used to construct the fourth order elastic tensor C_{ijkl} of each primary particle.

Consistent with measurements [31], the intergranular fracture energy $G_{\rm wf}$ was in general taken to be $2\,{\rm Jm}^{-2}$. However, recognising the uncertainty in the measurements, we also report a parametric study over the range $0 \le G_{\rm wf} \le 5\,{\rm Jm}^{-2}$. Recall that intergranular fracture was modelled via a cohesive zone model of strength $T_{\max}$. This introduces a fracture length scale $\ell \equiv EG_{\rm wf}/T^2_{\max}$ with E a representative Young's modulus of the primary particles, here taken as the average Young's modulus over all crystallographic orientations. The existence of this length scale carries significance as follows. For $\ell \gg d$ fracture will occur in a diffuse manner with a damage zone that spreads over numerous grains such that fracture is primarily set by the cohesive strength $T_{\max}$. On the other hand, for $\ell \ll d$ the cohesive zone model reduces to traditional linear elastic fracture mechanics (LEFM) with $G_{\rm wf}$ being the only relevant material parameter characterising the fracture process. For a well-sintered secondary particle, $T_{\max} \approx 10$ GPa is on the order of the theoretical strength, and so $\ell \approx 4$ nm. Given that the size of NMC811 primary particles is on the order of ~ 300 nm [32], it is clear that $\ell/d \ll 1$. This strongly suggests that fracture of the secondary particle is governed by LEFM. Thus, failure/fracture of the secondary particle is expected to be dictated by $G_{\rm wf}$ with $T_{\max}$ serving as a numerical regularisation parameter in the context of the cohesive zone model. All calculations reported here use $T_{\max} = 7.5$ GPa. This strength should not

Table 1
The elastic constants for the transversely isotropic NMC811 single crystal [30].

Elastic constant	Value
E_a	204 GPa
E_c	163 GPa
G_{ac}	59 GPa
ν_{ab}	0.34
ν_{ac}	0.21

be viewed as the theoretical grain boundary strength but rather the strength accounting for grain boundary defects such as impurities and micro-voids. This choice of parameters implies that, in these large-scale numerical calculations, we capture the energy release rates (that drive fracture) averaged over a grain boundary accurately but do not expect to capture the singular fields at the grain boundary junctions. This suffices to model the fracture of the secondary particle as fracture is expected to be propagation rather than initiation governed. The secondary particles are self-equilibrated and hence each grain boundary comprises a mixture of tensile and compressive tractions. Thus, just initiating a crack is insufficient to drive fracture of a grain boundary as the crack will be arrested by the compressive tractions.

Finally, we specify the lithiation strain $\boldsymbol{\varepsilon}^\theta$. For NMC811 single crystals, the lattice parameters $l_a^\theta = l_b^\theta$ and l_c^θ have been measured via X-ray diffraction [16] along the three crystallographic directions. In the initial state, the secondary particle is taken to be stress-free and fully lithiated. The lattice parameters at an occupancy of $\theta = 1$ are the reference values and $\boldsymbol{\varepsilon}^\theta$ vanishes at this value of occupancy. Consequently, the components of $\boldsymbol{\varepsilon}^\theta$ are given by

$$\varepsilon_a^\theta = \frac{l_a^\theta - l_a^{\theta=1}}{l_a^{\theta=1}}, \varepsilon_a^\theta = \varepsilon_b^\theta, \varepsilon_c^\theta = \frac{l_c^\theta - l_c^{\theta=1}}{l_c^{\theta=1}} \,. \tag{2}$$

A polynomial regression is used to obtain the functional dependence of $\boldsymbol{\varepsilon}^\theta$ upon θ from the measurements in Ref. [16] and this fit is shown in Fig. 3a. Whereas $\varepsilon_a^\theta = \varepsilon_b^\theta$ varies monotonically with θ, the lithiation strain along the c-axis has a peak value at an occupancy of $\theta \approx 0.33$. In addition, the dependence of volumetric strain $\varepsilon_a^\theta + \varepsilon_b^\theta + \varepsilon_c^\theta$ upon θ is included in Fig. 3a: the volumetric strain decreases monotonically upon delithiation, and upon full delithiation the single crystals have ~6 % lower volume compared to their fully lithiated state. A consequence of this volumetric reduction is that the density of NMC811 is nearly independent of the state of lithiation ranging from $\theta = 1$ to 0.1. The density of the NMC811 was thus assumed to be constant and equal to 4780 kg m^{-3}.

The CBD is modelled as a crushable plastic foam of modulus $E_{\text{CBD}} = 300$ MPa, Poisson's ratio $\nu_{\text{CBD}} = 0.3$ and strength $Y_{\text{CBD}} = 4$ MPa. Direct

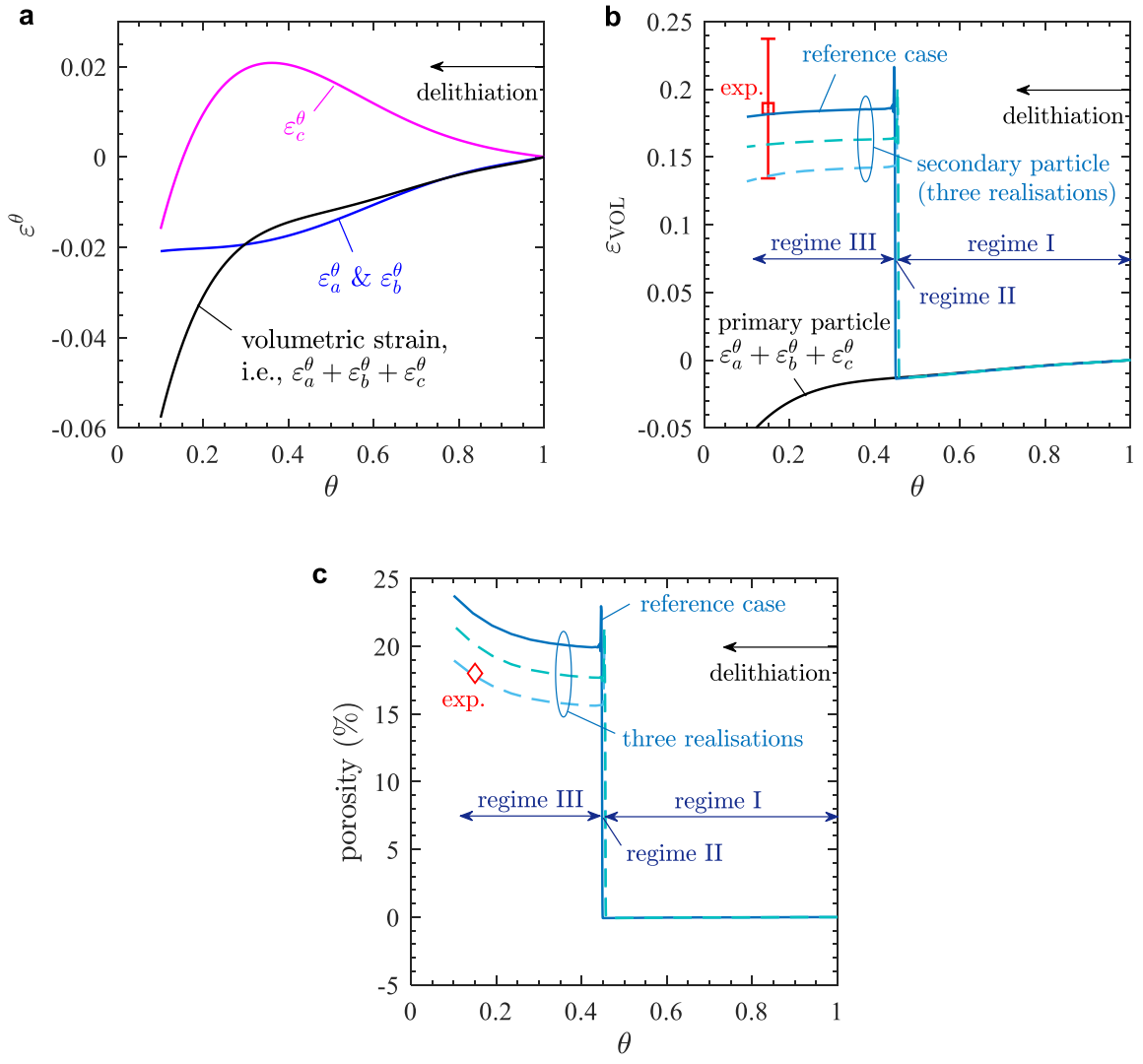

Fig. 3. (a) The lithiation strains $\varepsilon_a^\theta = \varepsilon_b^\theta$ and ε_c^θ along the a, b and c axes, respectively, of primary NMC811 particles as a function of the Li occupancy θ. The curves are fits through X-ray diffraction measurements reported in Märker et al. [16]. The corresponding volumetric strain $\varepsilon_a^\theta + \varepsilon_b^\theta + \varepsilon_c^\theta$ is included to illustrate that the primary particles monotonically shrink upon delithiation. Predictions of (b) overall volumetric strain ε_{VOL} and (c) porosity of the secondary particle as a function of θ starting from $\theta = 1$ for the case with $G_{\text{wf}} = 2$ Jm^{-2}. We show predictions for three random realisations of the secondary particle. The response is divided into three regimes as marked. The measurements of volumetric strain for the secondary particles [14] and individual primary particles [16] (that is, $\varepsilon_a^\theta + \varepsilon_b^\theta + \varepsilon_c^\theta$) are included in (b). The measurement of the average porosity within the cracked secondary particle from Li et al. [13] is included in (c).

measurements of the effective properties of the CBD are not available so we inferred these values as follows using established ideas [29] on the mechanical properties of porous solids. Taking typical values for a cathode of $f_P = 55\%$ and $f_V = 30\%$, it follows that the porosity of the CBD is $\rho_V \equiv f_V/(1 - f_P) = 0.67$. Then, the values E_{CBD} and Y_{CBD} follow from established relations [29] such that $E_{CBD} = E_M(1 - \rho_V)^2$ and $Y_{CBD} = 0.27Y_M(1 - \rho_V)^{1.5}$ where $E_M = 2.8$ GPa and $Y_M = 60$ MPa are the modulus and strength, respectively of the PVDF/carbon mixture material in the absence of porosity. The density of the CBD was assumed to be 590 kg m^{-3}.

2.5. Finite element calculations and size of the RVE

All calculations were performed in a dynamic finite element (FE) setting using the Explicit version of the commercial FE package ABAQUS. Since the delithiation process is slow, no dynamic effects are anticipated. However, we shall show that the secondary particle fragments dynamically on the scale of the primary particles. Thus, the calculations were performed in a dynamic setting. While experiments are performed at a C/50 rate, performing explicit dynamic calculations of 50 h duration is unrealistic. Instead, we selected a simulation time t_e such that dynamic effects are negligible prior to the initiation of catastrophic fracture of the secondary particle (i.e., the kinetic energy was less than 0.1 % of the strain energy of the RVE). Thus, t_e has no direct influence on the calculations as the spatially uniform Li concentration associated with the C/50 rate is directly imposed in our calculations.

We consider a representative spherical secondary particle of radius $R_P = 7.15\,\mu$m. While there is a large distribution of secondary particle sizes in the cathode (consistent with the composite sphere model), the X-ray tomographic observations reported in Ref. [14] focussed on particles of radii 5.1 μm to 8.9 μm and hence we have chosen a radius of $\sim 7\,\mu$m for our RVE analysis. The size and cost of the computation scales with the number of grains within the secondary particle. In order to keep this computational cost at a manageable level,[1] we chose to model $N = 400$ grains within the secondary particle consistent with the numerical model in Parks et al. [14]. This choice implies an average grain size of $d \approx 1.9\,\mu$m and, for the secondary particle shown in Fig. 2a, the grain sizes in the range $0.6\,\mu\text{m} < d_g < 2.8\,\mu\text{m}$. These grains are inevitably larger than the in real NMC811 secondary particles. However, with the fracture length scale $\ell \approx 4$ nm, these large grain sizes (i) imply that $\ell/d \ll 1$ and we remain in the LEFM governed fracture regime, and thus (ii) do not affect the key predictions related to the volume expansion.

For this secondary particle, we employed 250×10^3 continuum elements (C3D4 notation in ABAQUS) in the primary grains and the CBD. A further 37×10^3 cohesive elements (COH3D6 notation in ABAQUS) modelled the bonding between primary grains. The average continuum element size was approximately 0.4 μm.

3. Predictions of cracking upon delithiation

We proceed to present our numerical predictions in two steps. First, overall predictions are reported to make contact with observations and illustrate the fidelity of the approach. Second, the simulations are interrogated to extract physical insights into the cracking mechanisms that ultimately give rise to secondary particle expansion despite the fact that primary particles shrink upon delithiation. Unless otherwise specified, all calculations are presented for the reference parameters of fracture energy $G_{wf} = 2$ Jm^{-2} and a cathode of particle volume fraction $f_P = 55\%$ and porosity $f_V = 30\%$. The Coulomb friction co-efficient between the fractured grains was taken to be $\mu = 0.2$: spot calculations over the range $0.1 \le \mu \le 0.3$ were conducted to confirm that the primary observables reported here are insensitive to the choice of friction co-efficient within this range.

3.1. Predictions of main observations

The main observation in experiments [14] is the volume of secondary particle and we first report predictions of this observable to make direct contact with measurements. Define the volume $V(\theta)$ of the secondary particle at a given Li occupancy θ as the volume inside the circumscribing surface of the secondary particle. With the initial volume of the secondary particle defined as $V_P = V(\theta = 1)$, the predicted volumetric strain is defined by $\varepsilon_{VOL}(\theta) = V(\theta)/V_P - 1$. The predicted evolution of $\varepsilon_{VOL}(\theta)$ is included in Fig. 3b for three random realisations of the secondary particle and in all cases can be divided into three distinct regimes as marked in Fig. 3b:

- Regime I ($0.45 < \theta \le 1$): the volumetric strain of the secondary particle follows that of the primary particles (included in Fig. 3b) indicating negligible intergranular fracture. However, the orientation mismatch between the primary particles combined with the highly anisotropic elastic and lithiation properties implies that there is significant build-up of stress within the secondary particles as seen in Fig. 4 for the reference particle case marked in Fig. 3b. In Fig. 4, we include distributions of the von-Mises stress and principal stress $\sigma_{max} \equiv \sigma_1$ where the three principal stresses are ordered as $|\sigma_1| > |\sigma_2| > |\sigma_3|$.
- Regime II ($\theta \approx 0.45$): at $\theta \approx 0.45$, comminution of the secondary particle occurs, and is accompanied by a sudden increase in volume of the particle. We shall subsequently show that comminution is a dynamic fracture event with the primary particles acquiring kinetic energy. The primary particles separate due to this dynamic event, thereby opening intergranular cracks and giving rise to expansion of the secondary particle.
- Regime III ($\theta < 0.45$): after the catastrophic fracture event, nearly all primary particles are decoupled from each other and the stresses within the secondary particle are now negligible (Fig. 4). Continued delithiation results in the primary particles straining independently and not interacting with each other. The small volume reduction of the secondary particle seen in Fig. 3b in Regime III is due to the volumetric shrinkage of each primary particle during delithiation. Various sections through the secondary particle after complete delithiation (i.e., $\theta = 0.1$) are shown in Fig. 5 (for the reference case marked in Fig. 3b) where the cracks and the separation between the primary grains (shaded black) are clearly observed.

These predictions agree with experiments [14] in two critical aspects: (i) fragmentation of the secondary particles is predicted in the absence of Li concentration gradients within the secondary particle and (ii) the cracking/fragmentation of the secondary particle results in an increase in volume of the secondary particle of ranging from 14 % to 19 % (Fig. 3b) for the three random realisations consistent with measurements reported in Parks et al. [14] that are included as an error bar in Fig. 3b. The predictions in Fig. 3b are used to calculate the porosity of the secondary particle and included in Fig. 3c as a function of the lithium occupancy θ. Li et al. [13] measured the porosity as a consequence of cracking of NMC811 secondary particle upon delithiation at a rate C/5. The measured porosity averaged over the entire particle is included in Fig. 3c and is again in good agreement with the predictions.

The fidelity of our model is further confirmed by noting that it also predicts the influence of the grain structure within the secondary particles. The fragmented cracking pattern seen in Fig. 5 is mainly a consequence of the random orientation of grains. Observations reported in Kim et al. [33] suggest that when a-axis of all the grains are radially aligned within the secondary particle, fragmentation is inhibited and delithiation is accompanied by the appearance of a few long

[1] We ran our computations on a 32-core node and each cracking simulation of the secondary particle with 400 grains required ~140 h of wall-clock time.

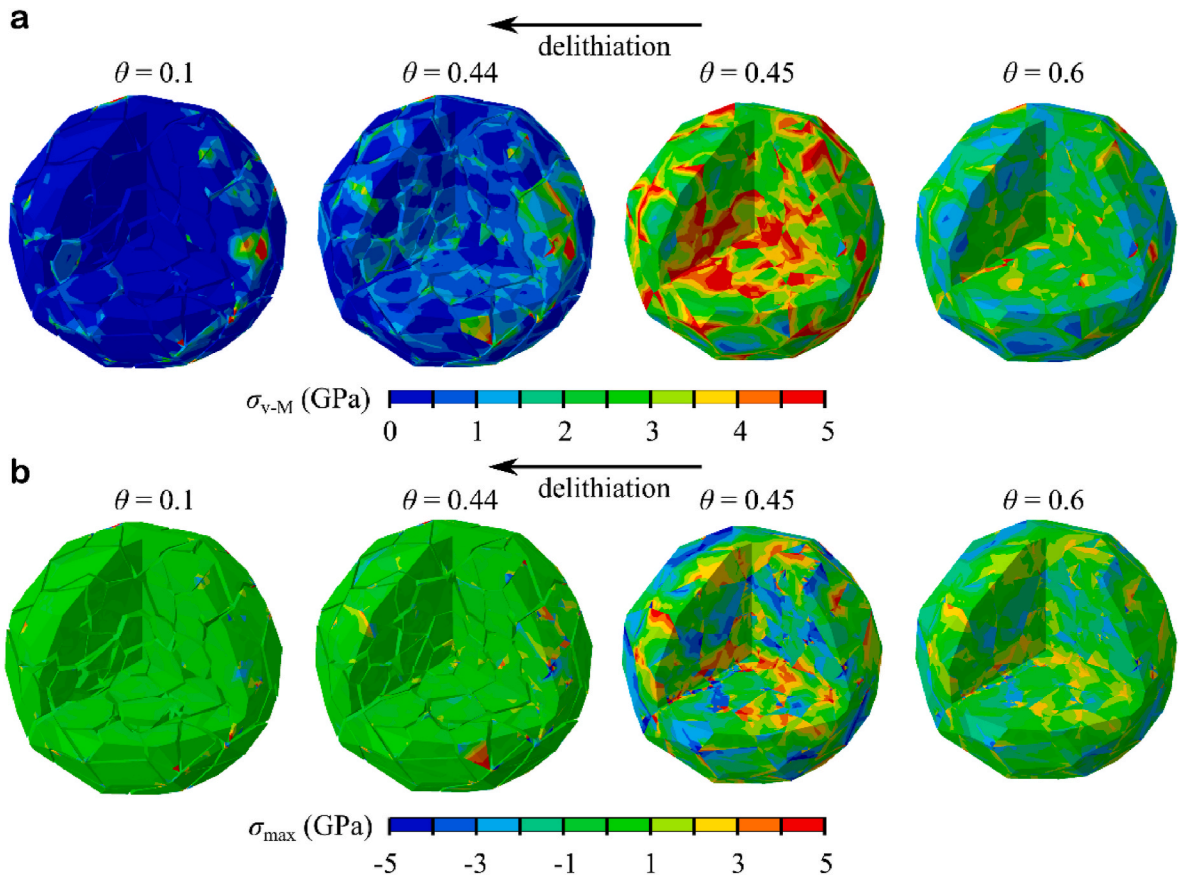

Fig. 4. Predictions of the evolution of (a) von-Mises stress and (b) principal stress σ_{max} within the secondary particle upon delithiation from $\theta = 1$ for the choice $G_{wf} = 2\,Jm^{-2}$ and the reference realisation of the secondary particle marked in Fig. 3b and c. Results are shown at four levels of lithiation θ: $\theta = 0.6$ corresponds to regime I; $\theta = 0.45$ and $\theta = 0.44$ in the vicinity of regime II, and $\theta = 0.1$ in regime III such that the particle has fractured and is nearly stress-free. The images of the secondary particle are shown with approximately a 1/8th section of the particle removed to visualise the interior of the secondary particle.

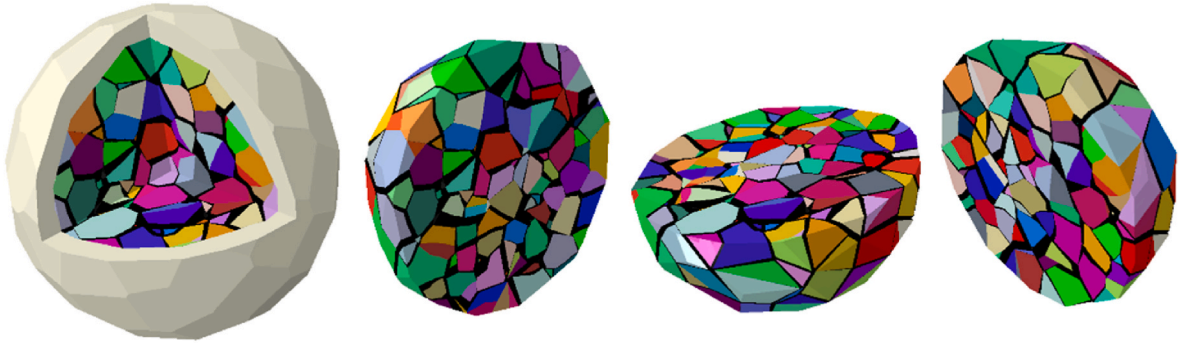

Fig. 5. A selection of sections through the fractured secondary particle to show the predicted cracking patterns. The cracks are shaded in black, and the primary particles are coloured in order to differentiate them. The predictions are given for the state $\theta = 0.1$, with the choice $G_{wf} = 2\,Jm^{-2}$ and the reference realisation of the secondary particle marked in Fig. 3b and c.

intergranular cracks. We performed additional simulations (Supplementary Fig. S1) for a secondary particle with *a*-axis of all the grains aligned along the radius of the spherical secondary particle (and *b*- and *c*-axes aligned randomly in the circumferential directions). Consistent with observations [33], our analysis predicts the absence of fragmentation and the appearance of a few dominant intergranular cracks (Supplementary Fig. S1). The fidelity of the predictions, as shown in Fig. 3 and also in Supplementary Fig. S1, implies that we can now use the simulations to interrogate the mechanisms of cracking.

3.2. The mechanism of dynamic fracture of the secondary particle

The main new insight reported above is that the expansion of the secondary particle is a consequence of dynamic fragmentation. We now investigate this in more detail by interrogating the transfer of mechanical energies during delithiation. All results are reported for the reference realisation of the secondary particle marked in Fig. 3b and c. The following five energies are involved: (i) the strain energy W_S of the RVE which primarily includes the elastic energy of the secondary particle but also comprises a small contribution from the elastic energy of the CBD; (ii) fracture energy W_Γ of the grain boundaries between the primary

particles; (iii) plastic dissipation W_{PL} of the CBD; (iv) frictional dissipation W_{F} between the primary particles and (v) kinetic energy W_{KE} of the RVE which is predominantly the kinetic energy of primary particles. To simplify the presentation of these energies, we define a material property that represents the total fracture energy of the secondary particle, $W_{\mathrm{wf}} \equiv G_{\mathrm{wf}} \sum_i A^{(i)}$ where $A^{(i)}$ is the area of the i^{th} facet between the primary particles and the summation is over all facets in the secondary particle. We shall present all energies normalised by W_{wf}, i.e., $\overline{W}_{\mathrm{S}} \equiv W_{\mathrm{S}}/W_{\mathrm{wf}}$, $\overline{W}_{\Gamma} \equiv W_{\Gamma}/W_{\mathrm{wf}}$ and so on.

Predictions of the evolution of all five normalised energies as θ drops from 1 to 0.1 are shown in Fig. 6a along with the three regimes of response as already mentioned in the context of Fig. 3b. In regime I, all energies except $\overline{W}_{\mathrm{S}}$ are zero and $\overline{W}_{\mathrm{S}}$ increases with decreasing θ. This strain energy build-up is due to the incompatibility of lithiation strain of adjacent primary grains; elastic strains (and stresses) are generated to maintain compatibility between the grains. With increasing delithiation the strain energy builds-up to approximately $8W_{\mathrm{wf}}$, denoting that the strain energy in the RVE is eight times that to fracture all grain boundaries of the secondary particle. At this stage, there is a catastrophic fracture event such that nearly all the grain boundaries shatter and all stored strain energy is released rapidly (this prediction is consistent with the acoustic emissions associated with fracture reported in the literature [34]).

Since the stored strain energy immediately prior to comminution much exceeds the energy required to fracture all grain boundaries, the excess energy is converted to a combination of kinetic energy, frictional dissipation and fracture energy, see the magnified view of the catastrophic fracture regime II in Fig. 6b where we now plot the temporal evolution of the energies to illustrate the dynamic nature of the fracture event (the plot shows that the energy is released over a period of $\approx$ 0.1 μs). After an initial rise, the kinetic energy decreases as it is dissipated in fracture energy and friction (which is the dominant dissipation mode). Finally, there is a third much less significant dissipation mode labelled plastic dissipation in Fig. 6. This refers to plastic dissipation associated with compression of the CBD surrounding the secondary particle in the RVE. As the secondary particle fractures and the primary particles acquire kinetic energy, they are forced to move apart which results in dilation of the secondary particle. This dilation of the secondary particle is confined by the compression of the CBD (which is modelled as a foam as it is porous). However, the energy dissipation in the CBD is relatively small with only about 6 % of the maximum strain energy of the secondary particle prior to fracture associated with the CBD compression resulting from ~20 % dilation of the secondary particle. Thus, small changes in the fracture process of the secondary particle associated with the precise microstructure of the secondary particle can cause relatively large changes in the predicted expansion (the predicted expansion ranges from 14 % to 19 % over the three realisations analysed; see Fig. 3b).

3.3. What sets the critical Li occupancy at which fragmentation occurs?

When θ has dropped to a value of 0.45 the total strain energy stored in the secondary particle far exceeds the fracture energy. This strain energy is released by a dynamic fracture event. *But what sets the critical Li occupancy fraction θ for the fracture event?* In order to gain additional insight into this, we consider (i) the dependence of the elastic stored energy W_{S} upon θ and then (ii) the dependence of energy release rate $\mathscr{G}_{\mathrm{B}}$ for fracture of a grain boundary upon θ.

Consider first the sensitivity of the elastic stored energy W_{S} upon θ assuming that the primary particles are rigidly and perfectly bonded to each other. The variation of $\overline{W}_{\mathrm{S}}$ is included in Fig. 7a. With decreasing θ starting from the $\theta = 1$ fully lithiated state, $\overline{W}_{\mathrm{S}}$ first increases due to increasing mismatch between $\varepsilon_a^\theta = \varepsilon_b^\theta$ and ε_c^θ (Fig. 3a). $\overline{W}_{\mathrm{S}}$ peaks at θ equal to ~ 0.33 and then diminishes as $\varepsilon_a^\theta = \varepsilon_b^\theta$ and ε_c^θ converge in value for $\theta < 0.33$. Not all of this strain energy is available to drive fracture and an understanding of the energy release rate $\mathscr{G}_{\mathrm{B}}$ provides insight into what sets the critical θ for the fracture event.

The secondary particle is a stochastic assembly of primary particles, and every grain boundary has a different value of energy release rate $\mathscr{G}_{\mathrm{B}}$. We calculate average $\mathscr{G}_{\mathrm{B}}^{(i)}$ of the i^{th} grain boundary with area $A^{(i)}$ as follows. For a given θ, $\mathscr{G}_{\mathrm{B}}^{(i)}(\theta)$ is defined as

$$\mathscr{G}_{\mathrm{B}}^{(i)}(\theta) \equiv -\frac{W_{\mathrm{S}}^{(i)}(\theta) - W_{\mathrm{S}}(\theta)}{A^{(i)}}, \tag{3}$$

where $W_{\mathrm{S}}^{(i)}(\theta)$ is the strain energy of the secondary particle at an Li occupancy θ with only the i^{th} grain boundary now traction-free (but allowed to sustain compressive contact stresses) and other grain boundaries remain intact. For each value of θ, we obtain a distribution of values of $\mathscr{G}_{\mathrm{B}}^{(i)}$ over all grain boundaries in the secondary particle and we

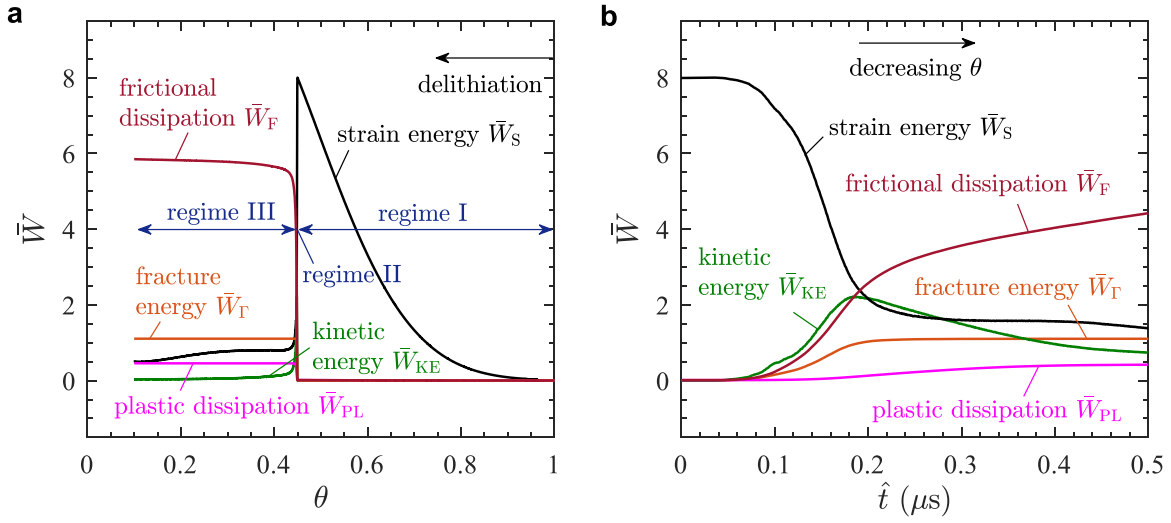

Fig. 6. (a) Predictions of the evolution of the five normalised energies $\overline{W}$ with Li occupancy θ upon delithiation starting from $\theta = 1$ for the case with $G_{\mathrm{wf}} = 2\,\mathrm{Jm}^{-2}$. The three regimes of behaviour are marked. (b) A zoom-in of the plot in (a) in regime II (around $\theta \sim 0.45$) when the catastrophic fracture event occurs. Here, we plot the temporal evolution of the energies with time $\hat{t} = 0$ at $\theta \sim 0.45$ and increasing with decreasing θ. All results are for the reference realisation of the secondary particle marked in Fig. 3b and c.

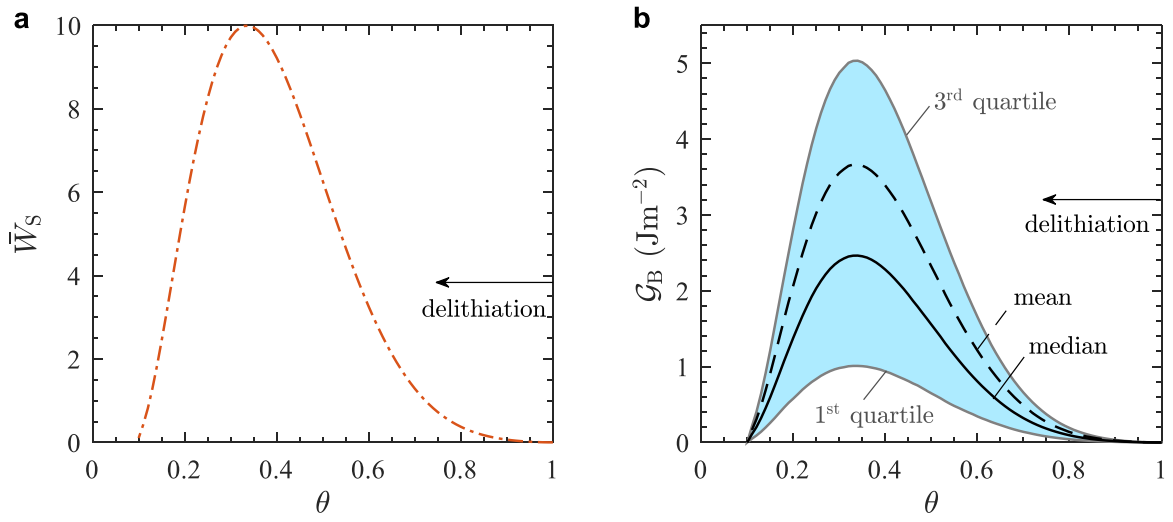

Fig. 7. (a) The variation of the normalised strain energy $\overline{W}_S$ of the RVE with Li occupancy θ with grain boundary fracture precluded. (b) Predictions of the energy release rate $\mathscr{G}_B$ of individual grain boundaries between primary grains in the secondary particle as a function of θ. For a given Li occupancy fraction θ, we calculate $\mathscr{G}_B$ for each grain boundary in the secondary particle assuming that all other boundaries remain intact. The three quartiles and the mean of the distribution over all grain boundaries are shown. Results in (a) and (b) are for the reference realisation of the secondary particle marked in Fig. 3b and c.

include these predictions in Fig. 7b (for the reference secondary particle indicated in Fig. 3b) in the form of three curves showing the quartiles of the energy release rates: the lower and upper lines represent the first and third quartiles while the middle line is the median of the distribution of $\mathscr{G}_B^{(i)}$. In addition, we include the mean of the distribution as a dashed line in the plot. Recall that the fracture energy is $G_{wf} = 2\,\mathrm{Jm}^{-2}$ and we observe that the median of $\mathscr{G}_B$, $\mathrm{Mdn}(\mathscr{G}_B) \approx G_{wf}$ at $\theta \approx 0.45$; this is when the secondary particle catastrophically fails. The surprising result is that $W_S \approx 8W_{wf}$ when this state is reached. We argue that this is the case because the secondary particle is essentially self-equilibrated such that there is a mixture of compressive and tensile tractions at the grain boundaries. The compressive tractions inhibit rather than promote fracture and this delays the fracture upon delithiation until $\theta \approx 0.45$. We emphasize that the use of the parameter $\mathscr{G}_B$ to estimate fracture is approximate since $\mathscr{G}_B$ is calculated by assuming only one fractured grain boundary with all other grain boundaries remaining intact. In reality, and in the full calculations reported in Fig. 3b, fractures of the vast majority of grain boundaries occur at $\theta \approx 0.45$ but nevertheless some fracture events occur earlier in the loading history (i.e., for $\theta > 0.45$). These early fractures change the elastic field within the secondary particle, and this is not considered in the calculations of Fig. 7b. However, the simplistic view of calculating $\mathscr{G}_B$ by ignoring history dependence does give significant insight into what sets the Li occupancy fraction for catastrophic fracture: the total strain energy must build-up to a sufficiently large value in order for the grain boundary energy release rate to attain the fracture energy for the majority of grain boundaries.

The above argument suggests that increasing the fracture energy to $G_{wf} > 2\,\mathrm{Jm}^{-2}$ will delay the onset of catastrophic fracture to $\theta < 0.45$. Additional calculations were performed for $2\,\mathrm{Jm}^{-2} < G_{wf} \leq 5\,\mathrm{Jm}^{-2}$ and the predictions of $\varepsilon_{VOL}(\theta)$ are given in Fig. 8 for the reference realisation of the secondary particle marked in Fig. 3b. The critical value of θ for the onset of catastrophic fracture (as parameterised by the sudden increase in ε_{VOL}) decreases slightly with increasing G_{wf} but more significantly the final value of ε_{VOL} after catastrophic fracture reduces with increasing G_{wf}. This is because a large fraction of the stored strain energy (that is independent of G_{wf}) goes into work of fracture leaving less energy to plastically compress the CBD. Additionally, for $G_{wf} \geq 5\,\mathrm{Jm}^{-2}$ catastrophic fracture of the secondary particle does not accompany full delithiation. This can be rationalised by observing from Fig. 7b that the

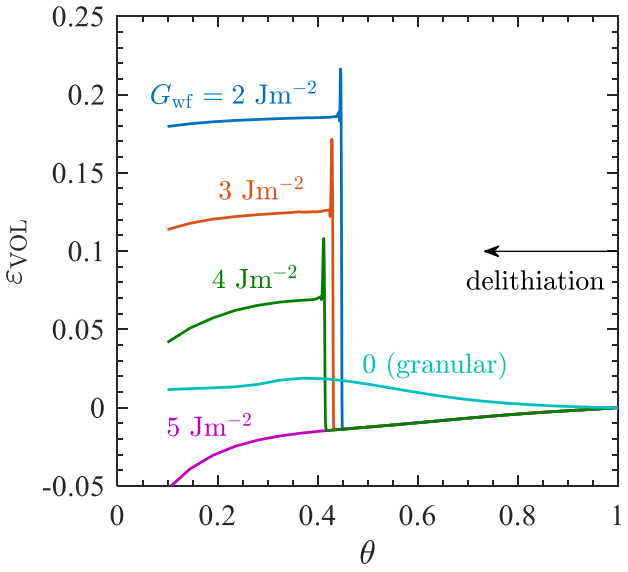

Fig. 8. Predictions of the evolution of the overall volumetric strain ε_{VOL} of the secondary particle as a function of θ upon delithiation starting from $\theta = 1$. Results are shown for grain boundary fracture energies in the range $0 \leq G_{wf} \leq 5\,\mathrm{Jm}^{-2}$ and the reference realisation of the secondary particle marked in Fig. 3b and c.

maximum upper quartile energy release rate is $\sim 5\,\mathrm{Jm}^{-2}$ and thus when $G_{wf} \geq 5\,\mathrm{Jm}^{-2}$, comminution of the secondary particle is precluded.

In summary, the dilation of the secondary particle upon fracture is associated with the dynamic release of strain energy that far exceeds the total fracture energy of all the grain boundaries. To more clearly illustrate this, we consider the limit of a "granular" secondary particle with $G_{wf} = 0$, i.e., the primary particles are not bonded to each other such that they can slide and separate freely with respect to each other but cannot interpenetrate akin to a granular medium. Prediction of $\varepsilon_{VOL}(\theta)$ for this limiting case is included in Fig. 8. As the primary particles delithiate and thereby volumetrically shrink (recall Fig. 3a), adjacent

primary particles deform in an incompatible manner (due to the anisotropic lithiation strains) and this opens cracks or gaps between the particles. This resembles the deformation of an over-consolidated granular medium where macroscopic strain is accompanied by dilation [35]. However, the degree of dilation in the granular limit is small compared to the case where dynamic fracture of the secondary particles occurs, as discussed above.

4. Concluding remarks

The cracking of $LiNi_{0.8}Mn_{0.1}Co_{0.1}O_2$ (known as NMC811) secondary particles within a cathode during delithiation is analysed by considering a representative volume element comprising a single secondary particle embedded within the porous carbon and binder domain. The secondary particle is modelled as a bonded polycrystal of single crystal primary particles connected to each other via cohesive surfaces that model the intergranular interactions and fracture. Attention is restricted to low C-rates such that the lithium concentration within the secondary particle is spatially uniform.

We demonstrate that the anisotropic lithiation strains of the single crystal primary particles result in incompatible deformation between adjacent grains which in turn results in the generation of large elastic stresses and strains. The associated build-up of strain energy induces intergranular fracture when the grain boundary energy release rate attains the fracture energy. Consistent with observations, fracture can occur even at very low C-rates due to the anisotropic lithiation strains of the primary particles. The critical grain boundary energy release rates to fracture the bond between primary particles are attained when the total strain energy of the secondary particle is far greater than the total fracture energy of all the grain boundaries. Thus, fragmentation of the secondary particle is a sudden, dynamic and catastrophic event and occurs when the lithium occupancy is about 0.45. The consequent released strain energy is converted to kinetic energy of the primary particles which then move apart while being constrained by the surrounding porous carbon and binder domain. The predictions, much in line with observations, suggest that the secondary particle expands in volume by approximately 20 %. Moreover, the dynamic nature of the fracture is consistent with numerous observations of acoustic emissions that accompany the fracture of secondary particles.

Our predictions suggest that the NMC811 secondary particles, atleast at low C-rates, will remain intact if the intergranular fracture energy exceeds about 5 Jm^{-2}. This provides clear guidance for processing routes (e.g., improved sintering and/or grain boundary engineering) in order to improve the degradation performance of NMC811 cathodes. Moreover, our model predicts that fracture occurs catastrophically at an Li occupancy of 0.45 with negligible change in secondary particle volume above and below this occupancy. This prediction awaits experimental verification. Finally, our work here is restricted to low C-rates where spatial variations in the Li concentration vanish. While these low C-rates provide physical insight, the implications of the fracture mechanisms revealed here for the more practical higher C-rates require investigations in future studies.

CRediT authorship contribution statement

S.S. Shishvan: Conceptualization, Methodology, Investigation, Software, Validation, Formal analysis, Visualization, Writing – review & editing. **N.A. Fleck:** Validation, Writing – review & editing. **R.M. McMeeking:** Validation, Writing – review & editing. **V.S. Deshpande:** Conceptualization, Investigation, Supervision, Validation, Writing – original draft.

Declaration of competing interest

The authors declare that they have no known competing financial interests or personal relationships that could have appeared to influence the work reported in this paper.

Data availability

No data was used for the research described in the article.

Appendix A. Cohesive zone model for intergranular fracture

The traction-separation law to model grain boundary fracture is schematically illustrated in Fig. 2d and here we summarise this model. Define the mode I normal traction between the grains as T^{n}, the mode II shear traction in the direction of crack growth as T^{s} and the mode III shear traction T^{t}. The corresponding normal and shear separations are denoted by δ^{n}, δ^{s} and δ^{t}, respectively. The cohesive relationship between the primary grains is defined in two steps: (i) the initial, undamaged traction-separation relation such that the damage variable $D = 0$, and (ii) a softening relation after the onset of damage with $0 < D \leq 1$. The traction separation relation takes the form

$$\begin{aligned} T^{\mathrm{n}} &= \begin{cases} (1-D)K\delta^{\mathrm{n}} & \delta^{\mathrm{n}} \geq 0, \\ K\delta^{\mathrm{n}} & \text{otherwise}, \end{cases} \\ T^{\mathrm{s}} &= (1-D)K\delta^{\mathrm{s}}, \\ T^{\mathrm{t}} &= (1-D)K\delta^{\mathrm{t}}, \end{aligned} \tag{A1}$$

where K is a stiffness. Note that damage does not affect the normal traction when $\delta^{\mathrm{n}} < 0$, i.e., compressive interactions between grains. In the undamaged state (at the beginning of the calculation), the damage variable $D = 0$ and no damage develops until

$$\max\{\langle T^{\mathrm{n}}\rangle, |T^{\mathrm{s}}|, |T^{\mathrm{t}}|\} = T_{\max}, \tag{A2}$$

where $< >$ represents the Macaulay bracket so that (A2) implies that compression does not initiate damage. After the initiation of damage, the evolution law for D is based upon the assumption that the tractions decrease linearly with increasing separation. Define an effective separation $\Delta \equiv \sqrt{\langle\delta^{\mathrm{n}}\rangle^2 + (\delta^{\mathrm{s}})^2 + (\delta^{\mathrm{t}})^2}$ and denote the value of this effective displacement at the initiation of damage by Δ_0. The damage variable is then given by

$$D = \begin{cases} \dfrac{\Delta_{\mathrm{f}}(\Delta_{\max} - \Delta_0)}{\Delta_{\max}(\Delta_{\mathrm{f}} - \Delta_0)} & \Delta_{\max} \leq \Delta_{\mathrm{f}} \\ 1 & \text{otherwise}, \end{cases} \tag{A3}$$

where Δ_{max} is the maximum value of the effective separation Δ attained during the loading history and Δ_f is a material parameter that sets the value of Δ when complete fracture occurs, i.e., when $D = 1$. Thus, Δ_f is related to the grain boundary fracture energy and we set $\Delta_f - \Delta_0 \equiv 2G_{wf}/T_{max} - T_{max}/K$ so that area under the traction displacement curve equals G_{wf}.

The values of T_{max} and G_{wf} are given in Section 2.4. We choose $K \approx 200E/d$ where $E \approx 190$ GPa is a representative Young's modulus of the primary particles here taken as the average Young's modulus over all crystallographic orientations of the primary particle and $d = 1.9\ \mu$m is the average size of the primary particles. This choice of K ensures that the intergranular stiffness has a negligible influence on the overall moduli of the secondary particle.

Appendix B. Compressible inelastic model for the CBD

The porous CBD is modelled as a crushable foam using the Deshpande and Fleck [27] model. This model while originally developed for metal foams has been extensively applied [28] to polymer foams with a porosity similar to the CBD and in fact has been implemented in commercial FE codes such as ABAQUS primarily for use to model polymer foams. Write the deviatoric stress as $s_{ij} \equiv \sigma_{ij} - (\sigma_{kk}/3)\delta_{ij}$ where δ_{ij} denotes the Kronecker delta. Then, the isotropic yield surface of the foam is specified in terms of the uniaxial yield strength σ_0 by

$$\Phi \equiv \widehat{\sigma} - \sigma_0 = 0. \tag{B1}$$

Here, the effective stress $\widehat{\sigma}$ is a function of the von-Mises stress $q \equiv \sqrt{(3/2)s_{ij}s_{ij}}$ and mean stress $\sigma_m \equiv \sigma_{kk}/3$ according to

$$\widehat{\sigma}^2 \equiv \frac{1}{1+(\alpha/3)^2}\left(q^2 + \alpha^2\sigma_m^2\right)^2, \tag{B2}$$

where the material parameter α is the ratio of deviatoric to hydrostatic strength. The plastic strain rate $\dot{\varepsilon}^p_{ij}$ obeys an associated flow rule such that

$$\dot{\varepsilon}^p_{ij} \equiv \dot{\widehat{\varepsilon}}\frac{\partial \Phi}{\partial \sigma_{ij}}. \tag{B3}$$

The effective plastic strain rate $\dot{\widehat{\varepsilon}}$ is work-conjugate to $\widehat{\sigma}$ and can be written in terms of the deviatoric plastic strain rate $\dot{\varepsilon}'_{ij} \equiv \dot{\varepsilon}^p_{ij} - \delta_{ij}\dot{\varepsilon}^p_{kk}$ and the volumetric plastic strain rate $\dot{\varepsilon}_m \equiv \dot{\varepsilon}^p_{kk}$ as

$$\dot{\widehat{\varepsilon}}^2 \equiv \left[1+(\alpha/3)^2\right]\left(\dot{\varepsilon}_e^2 + \frac{1}{\alpha^2}\dot{\varepsilon}_m^2\right)^2, \tag{B4}$$

where $\dot{\varepsilon}_e \equiv \left[(2/3)\dot{\varepsilon}'_{ij}\dot{\varepsilon}'_{ij}\right]^{1/2}$. It remains to specify the strain hardening response. The uniaxial yield strength σ_0 is a function of $\widehat{\varepsilon}$ and is specified to emulate a foam response (Fig. 2e) comprising a stress plateau followed by densification modelled by a linearly hardening response. Consequently, σ_0 as a function of $\widehat{\varepsilon}$ if given by

$$\sigma_0 = \begin{cases} Y_{CBD} & \widehat{\varepsilon} \le \varepsilon^D_{CBD} \\ Y_{CBD} + E_M\left(\widehat{\varepsilon} - \varepsilon^D_{CBD}\right) & \text{otherwise.} \end{cases} \tag{B5}$$

The specification of the constitutive model is completed by assuming an additive decomposition of the elastic and plastic strain rates so that the total strain rate is given by $\dot{\varepsilon}_{ij} = \dot{\varepsilon}^{EL}_{ij} + \dot{\varepsilon}^p_{ij}$. Here, we assume that the elastic strain rate $\dot{\varepsilon}^{EL}_{ij}$ is specified by the isotropic Hooke's law in terms of the Young's modulus $E_{CBD} \ll E_M$ and Poisson ratio ν_{CBD}.

The material parameters Y_{CBD}, ε^D_{CBD}, E_{CBD}, ν_{CBD} and E_M are provided in Section 2.4. Consistent with the usual convention for highly porous solids, we set $\alpha = 3/\sqrt{2}$ [28] such that the plastic Poisson's ratio of the CBD is zero: this value of plastic Poisson's ratio has been shown in numerous studies, e.g. Deshpande and Fleck [28], on polymer foams to be appropriate and in the absence of equivalent data for the CBD we take this as a best guess.

Appendix C. Supplementary data

Supplementary data to this article can be found online at https://doi.org/10.1016/j.jpowsour.2023.233745.

References

[1] S.-T. Myung, F. Maglia, K.-J. Park, C.S. Yoon, P. Lamp, S.-J. Kim, Y.-K. Sun, Nickel-rich layered cathode materials for automotive lithium-ion batteries: achievements and perspectives, ACS Energy Lett. 2 (2017) 196–223.

[2] Y. Zhao, P. Stein, Y. Bai, M. Al-Siraj, Y. Yang, B.-X. Xu, A review on modeling of electro-chemo-mechanics in lithium-ion batteries, J. Power Sources 413 (2019) 259–283.

[3] V.S. Deshpande, R.M. McMeeking, Models for the interplay of mechanics, electrochemistry, thermodynamics, and kinetics in Lithium-Ion Batteries, Appl. Mech. Rev. 75 (2023), 010801.

[4] J. He, J. Meng, Y. Huang, Challenges and recent progress in fast-charging lithium-ion battery materials, J. Power Sources 570 (2023), 232965.

[5] X. Zhang, W. Shyy, A.M. Sastry, Numerical simulation of intercalation-induced stress in Li-ion battery electrode particles, J. Electrochem. Soc. 154 (2007). A910–A916.

[6] K. Zhao, M. Pharr, J.J. Vlassak, Z. Suo, Fracture of electrodes in lithium-ion batteries caused by fast charging, J. Appl. Phys. 108 (2010), 073517.

[7] R.T. Purkayastha, R.M. McMeeking, A linearized model for lithium-ion batteries and maps for their performance and failure, ASME J. Appl. Mech. 79 (2012), 031021.

[8] R.T. Purkayastha, R.M. McMeeking, A parameter study of intercalation of lithium into storage particles in a lithium-ion battery, Comput. Mater. Sci. 80 (2013) 2–14.

[9] W.H. Woodford, Y.M. Chiang, W.C. Carter, Electrochemical shock of intercalation electrodes – a fracture mechanics analysis, J. Electrochem. Soc. 157 (2010). A1052–A1059.

[10] W.H. Woodford, Y.M. Chiang, W.C. Carter, Design criteria for electrochemical shock resistant battery electrodes, Energy Environ. Sci. 5 (2012) 8014–8024.

[11] W.H. Woodford, Y.M. Chiang, W.C. Carter, Electrochemical shock in ion-intercalation materials with limited solid-solubility, J. Electrochem. Soc. 160 (2013) A1286–A1292.

[12] A.O. Kondrakov, A. Schmidt, J. Xu, H. Geßwein, R. Monig, P. Hartmann, H. Sommer, T. Brezesinski, J. Janek, Anisotropic lattice strain and mechanical

degradation of high- and low-nickel NCM cathode materials for Li-ion batteries, J. Phys. Chem. 121 (2017) 3286–3294.
[13] S. Li, Z. Jiang, J. Han, Z. Xu, C. Wang, H. Huang, C. Yu, S.-J. Lee, P. Pianetta, H. Ohldag, J. Qiu, J.-S. Lee, F. Lin, K. Zhao, Y. Liu, Mutual modulation between surface chemistry and bulk microstructure within secondary particles of nickel-rich layered oxides, Nat. Commun. 11 (2020) 4433.
[14] H.C.W. Parks, A.M. Boyce, A. Wade, T.M.M. Heenan, C. Tan, E. Martínez-Pañeda, P.R. Shearing, D.J.L. Brett, R. Jervis, Direct observations of electrochemically induced intergranular cracking in polycrystalline NMC811 particles, J. Mater. Chem. A (2023), https://doi.org/10.1039/d3ta03057a.
[15] H.-H. Ryu, K.-J. Park, C.S. Yoon, Y.-K. Sun, Capacity fading of Ni-rich Li $[Ni_xCo_yMn_{1-x-y}]O_2$ ($0.6 \leq x \leq 0.95$) cathodes for high-energy-density lithium-ion batteries: bulk or surface degradation? Chem. Mater. 30 (2018) 1155–1163.
[16] K. Märker, P.J. Reeves, C. Xu, K.J. Griffith, C.P. Grey, Evolution of structure and lithium dynamics in LiNi0.8Mn0.1Co0.1O2 (NMC811) cathodes during electrochemical cycling, Chem. Mater. 31 (2019) 2545–2554.
[17] M. Zhu, J. Park, A.M. Sastry, Fracture analysis of the cathode in Li-ion batteries: a simulation study, J. Electrochem. Soc. 159 (2012) A492–A498.
[18] G. Sun, T. Sui, B. Song, H. Zheng, L. Lu, A.M. Korsunsky, On the fragmentation of active material secondary particles in lithium ion battery cathodes induced by charge cycling, Extreme Mech. Lett. 9 (2016) 449–458.
[19] J.M. Allen, P.J. Weddle, A. Verma, A. Mallarapu, F. Usseglio-Viretta, D.P. Finegan, A.M. Colclasure, W. Mai, V. Schmidt, O. Furat, D. Diercks, T. Tanim, K. Smith, Quantifying the influence of charge rate and cathode-particle architectures on degradation of Li-ion cells through 3D continuum-level damage models, J. Power Sources 512 (2021), 230415.
[20] M. Klinsmann, D. Rosato, M. Kamlah, R.M. McMeeking, Modeling crack growth during Li extraction in storage particles using a fracture phase field approach, J. Electrochem. Soc. 163 (2016) A102–A118.
[21] M.E. Ferraro, B.L. Trembacki, V.E. Brunini, D.R. Noble, S.A. Roberts, Electrode mesoscale as a collection of particles: coupled electrochemical and mechanical analysis of NMC cathodes, J. Electrochem. Soc. 167 (2020), 013543.
[22] A.M. Boyce, E. Martínez-Pañeda, A. Wade, Y.S. Zhang, J.J. Bailey, T.M. Heenan, D. J.L. Brett, P.R. Shearing, Cracking predictions of lithium-ion battery electrodes by X-ray computed tomography and modelling, J. Power Sources 526 (2022), 231119.
[23] Z. Yang, H. Charalambous, Y. Lin, S.E. Trask, L. Yu, J. Wen, A. Jansen, Y. Tsai, K. M. Wiaderek, Y. Ren, I. Bloom, Extreme fast charge aging: correlation between electrode scale and heterogeneous degradation in Ni-rich layered cathodes, J. Power Sources 521 (2022), 230961.
[24] Z. Hashin, Analysis of composite materials – a survey, J. Appl. Mech. 50 (1983) 481–505.
[25] R. Quey, P.R. Dawson, F. Barbe, Large-scale 3D random polycrystals for the finite element method: generation, meshing and remeshing, Comput. Methods Appl. Mech. Eng. 200 (2011) 1729–1745.
[26] S. Pandurangi, D.S. Hall, C.P. Grey, V.S. Deshpande, N.A. Fleck, Chemo-mechanical analysis of lithiation/delithiation of Ni-rich single crystals, J. Electrochem. Soc. 170 (2023), 050531.
[27] V.S. Deshpande, N.A. Fleck, Isotropic constitutive model for metallic foams, J. Mech. Phys. Solid. 48 (2000) 1253–1276.
[28] V.S. Deshpande, N.A. Fleck, Multi-axial yield behavior of polymer foams, Acta Mater. 49 (2001) 1859–1866.
[29] L.J. Gibson, M.F. Ashby, Cellular Solids, Structure and Properties, second ed., Cambridge University Press, Cambridge UK, 1997.
[30] H. Sun, K. Zhao, Electronic structure and comparative properties of LiNixMnyCozO2 cathode materials, J. Phys. Chem. C 121 (2017) 6002–6010.
[31] J.C. Stallard, L. Wheatcroft, S.G. Booth, R. Boston, S.A. Corr, M.F.L. De Volder, B. J. Inkson, N.A. Fleck, Mechanical properties of cathode materials for lithium-ion batteries, Joule 6 (2022) 9884, 1007.
[32] H.-J. Noh, S. Youn, C.S. Yoon, Y.-K. Sun, Comparison of the structural and electrochemical properties of layered $Li[Ni_xCo_yMn_z]O2$ ($x = 1/3$, 0.5, 0.6, 0.7, 0.8 and 0.85) cathode material for lithium-ion batteries, J. Power Sources 233 (2013) 121–130.
[33] U.-H. Kim, G.-T. Park, B.-K. Son, G.W. Nam, J. Liu, L.-Y. Kuo, P. Kaghazchi, C. S. Yoon, Y.-K. Sun, Heuristic solution for achieving long-term cycle stability for Ni-rich layered cathodes at full depth of discharge, Nat. Energy 5 (2020) 860–869.
[34] H. Michael, R.E. Owen, J.B. Robinson, T.M.M. Heenan, C. Tan, A.J. Wade, R. Jervis, D.J.L. Brett, P.R. Shearing, Correlative electrochemical acoustic time-of-flight spectroscopy and X-ray imaging to monitor the performance of single-crystal and polycrystalline NMC811/Gr lithium-ion batteries, J. Power Sources 542 (2022), 231775.
[35] R.M. Nedderman, Statics and Kinematics of Granular Materials, Cambridge University Press, Cambridge UK, 2005.